IEEE Robotics and Automation Letters (RA-L) paper, presented at ICRA 2026, Vienna, Austria. Cite as RA-L paper.

A Miniaturized Tendon-Driven Continuum Robot for Direct Laser Deposition

Luca Raimondi, Matteo Russo, *Member, IEEE*, Xin Dong, Andy Norton, and Dragos Axinte

***Abstract*—Direct laser deposition, a form of additive manufacturing, shows potential in numerous high-value applications such as aeroengine blade repair. However, conventional setups are bulky and unsuitable for in-situ repair, requiring costly engine disassembly. This letter presents a miniaturized high-repeatability tendon-driven robot that showed good potential for delivering additive manufacturing equipment for in-situ processes like direct laser deposition. The integrated actuation and ruggedized control unit make the robot portable and compatible with various aeroengines. The actuation design prevents excessive fiber optic bending and damage. While continuum robots have the advantage of flexible and redundant structures, they often lack accuracy and repeatability. The optimized kinematics and actuation of the robot presented permitted to achieve in controlled laboratory conditions an excellent repeatability with a standard deviation of 0.02 mm on a linear path and below 0.1 mm on a path that simulates the reconstruction of a blade. The robot showed excellent linearity on each segment of the path with a coefficient of determination to the 3D best-fit line of 0.999, while maintaining the commanded end effector velocity magnitude with a standard deviation of 0.05 mm/s along the whole path.**

***Index Terms*—Compliant joints and mechanisms, mechanism design, tendon/wire mechanism.**

I. Introduction

WHEN an aeroengine blade is damaged and an indentation is formed, it can be beneficial to remove the defect to prevent stress concentration factors that could reduce service life. This task is conventionally carried out using slender grinding and polishing tools inserted into the engine through an inspection port, called borescope port [1]. Then, it would be beneficial to reconstruct the blade profile using, for example, additive manufacturing (AM) technologies.

Direct Laser Deposition (DLD), a variant of Directed Energy Deposition (DED), is a specialized form of AM that employs a laser source to fuse materials by melting them as they are deposited. This process is usually performed layer by layer, feeding materials in the form of metallic powder or wire into a small melt pool. This technique allows for the production of intricate 3D structures [2] and in recent years attracted the interest of the aerospace industry for its potential in repairing aeroengines with great advantages in terms of cost saving and environmental footprint [3], [4] compared to replace the whole blade. Since then, multiple studies concluded the suitability in carrying out successful repairs in terms of geometry reconstruction [5], [6] and metallurgical and mechanical properties [7], [8].

Despite examples of miniaturized laser heads have been described in the literature, all the setups used for DLD are bulky and require the engine to be disassembled to extract the blades to be repaired [5]. This greatly increases the downtime and costs associated with the repair. A different approach is considered in in-situ repair, in which the operation is carried out without disassembling the component. In the case of aeroengines, trained technicians can perform precise interventions within the engine by accessing it through inspection ports known as borescope ports [9]. As attractive as this option may appear, training technicians and developing tools to perform complex maintenance operations within the narrow and intricate environment of an aeroengine is a challenging task. Even when feasible, the success of such interventions heavily depends on the operator's skill. Developing automated systems to support technicians and reduce repair time would be highly beneficial [10]. While such scenarios are often inaccessible to conventional industrial manipulators, continuum robots, thanks to their flexible backbones capable of continuous bending, can navigate complex curved paths. Their slender form factor, with cross-sections as small as a few millimetres, allows access to extremely confined spaces [10]. A few examples of robots using this design for in-situ repair of aeroengine components have already been presented, including a system for flame spraying [11] and one for boreblending of damaged blades [1], [9]. In the first case, the bulky actuation system requires heavy support structures to position the robot near the engine. Moreover, the relatively large arm diameter and the high number of degrees of freedom, which can limit repeatability, make it unsuitable for high-precision manufacturing in confined spaces. In the second case, the absence of an internal actuation channel, with cables entering from the side, would result in excessive bending and potential damage to the optical fibre used for the laser.

However, current continuum robots for aerospace focus on their slender size and redundancy to navigate the environment [12], [13] with a satisfactory precision (1-5 mm) rather than leveraging their form factor to perform high-precision (0.01-0.1 mm) manufacturing tasks in enclosed environments.

Continuum robots have also found applicability in other sectors that share similar requirements of minimally invasive operations, such as surgical robotics [14], [15]. However, these

Received 28 February 2025; accepted 26 July 2025. Date of publication 11 August 2025; date of current version 18 August 2025. This article was recommended for publication by Associate Editor Damiano Zanotto and Editor Clement Gosselin upon evaluation of the reviewers' comments. This work was supported by Innovate U.K. through the Aerospace Technology Institute (ATI) through Project REINSTATE under Grant 51689. *(Corresponding author: Dragos Axinte.)*

Luca Raimondi, Matteo Russo, Xin Dong, and Dragos Axinte are with Rolls-Royce UTC in Manufacturing and On-Wing Technology, University of Nottingham, NG72RD Nottingham, U.K. (e-mail: luca.raimondi@ukaea.uk; matteo.russo@uniroma2.it; xin.dong@nottingham.ac.uk; dragos.axinte@nottingham.ac.uk).

Andy Norton is with On-Wing Technology, Rolls-Royce PLC, DE24 9BD Derby, U.K. (e-mail: andy.norton@Rolls-Royce.com).

This article has supplementary downloadable material available at https://doi.org/10.1109/LRA.2025.3597509, provided by the authors.

Digital Object Identifier 10.1109/LRA.2025.3597509

IEEE Robotics and Automation Letters (RA-L) paper, presented at ICRA 2026, Vienna, Austria. Cite as RA-L paper.

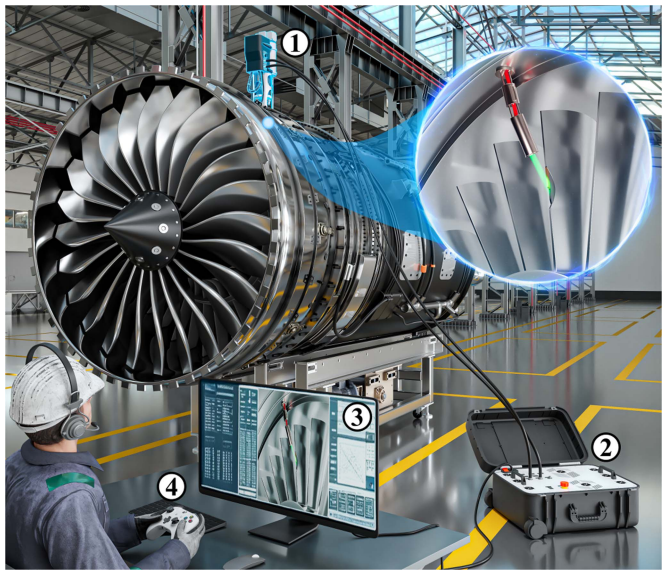

Fig. 1. Overview of the application (1: Robot installed on an aero engine, 2: Robot's control unit with motors controllers and real-time controller, 3: Host PC, 4: Operator controlling the robot using a joystick).

systems often present very large actuation units [16], [17] that, while acceptable in a surgical room, make them not suited for on-wing repair. An interesting design was presented in [18] in which an ultra-slender and portable tendon-driven robot was developed. The system, finding a variety of applications such as aerospace, nuclear, and robot-assisted surgery, exemplifies the versatility of continuum robots. However, while the length of the robot was beneficial for the applications proposed, it can be seen as a limiting factor for the repeatability of the end effector motion in a task such as DLD.

As this review highlights, despite the significant potential of continuum robots and extensive research efforts, no system currently exists that is suitable for the in-situ reconstruction of aeroengine blades. To address this gap, this letter presents a novel miniaturized tendon-driven robot for in-situ additive manufacturing (AM) repair. The articulated arm, with a diameter of only 8 mm, is capable of accessing the narrow inspection ports of an aeroengine. The robot's kinematic design has been optimized to minimize the number of degrees of freedom and reduce the arm length, thereby enhancing repeatability. An umbilical channel running through both the actuation system and articulated arm enables safe routing of the power and optical cables required by the end-effector, while preventing damage due to excessive bending. Finally, the portable nature of the robot and actuation unit allows deployment within minutes, facilitating practical on-wing applications. Section II describes the design of the robot, its control strategy, and kinematics details. Section III summarizes the extensive experimental validation to assess the robot's performance and suitability for the task. Finally, Section IV discusses and summarizes the work presented.

II. System Design and Operation

Fig. 1 provides an overview of the system and illustrates how an operator would use it to perform in-situ repair of a previously boreblended blade within an aeroengine. The robotic system is composed of five key elements:

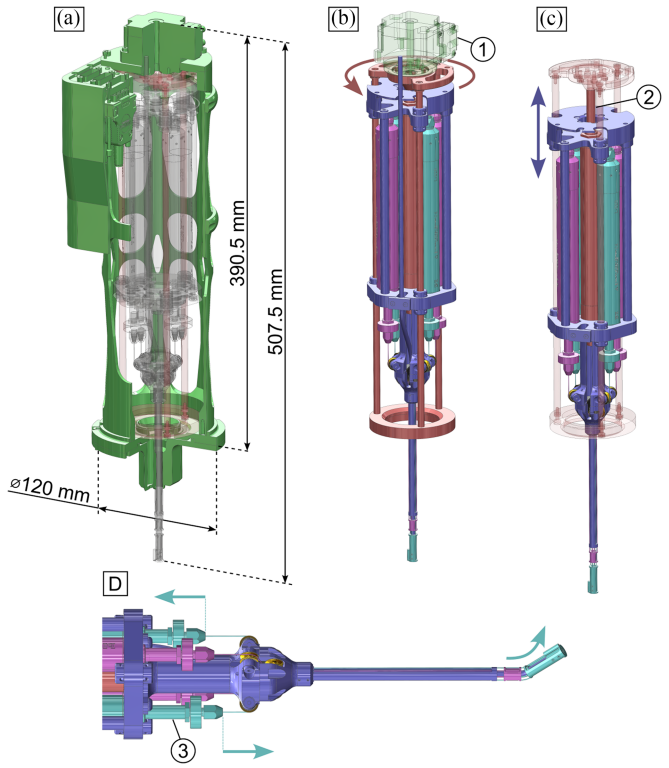

Fig. 2. Robot's key units and operating principle (A: Stationary chassis, B: Rotary chassis rotating relatively to the stationary chassis using a rotary actuator (1), C: Linear chassis translating relatively to the rotary chassis using a linear actuator (2), D: Detail of the actuation of the compliant joints through a pair of agonist and antagonist tendons actuated by linear actuators (3)).

- *Continuum robot with integrated actuation (1):* A two-DoF miniaturized tendon-driven robot with additional feed (translation) and twist (rotation) DoFs at the base.
- *Control unit (2):* A rugged, portable enclosure containing the real-time controller, motor drivers, and power supply. The front panel enables plug-and-play functionality.
- *Laser source:* This prototype uses an Arduino to power a laser diode and synchronize it with the robot via serial communication. The modular design with an external laser source was chosen to permit a seamless transition among different laser setups.
- *Host PC (3):* A PC handles low-priority LabVIEW tasks (e.g., GUI), while computationally intensive, time-critical code runs on the controller.
- *Human-Machine Interface (HMI) (4):* An Xbox joystick acting as a teach pendant, by allowing to control the robot and actuating the end-effector tool.

A. Design of the Manipulator

The design of the robot's actuation system and articulated arm, shown in Figs. 2 and 3, has been optimized for in-situ repair applications and to accommodate the routing of cables and the optical fibre required for AM tasks. As illustrated in Fig. 2, the robot consists of three key units: (A) an outer stationary chassis, (B) a rotary frame that provides the twist degree of freedom (DoF), and (C) a linear mechanism that supports the articulated arm and delivers the feed DoF. The robot actuation is 390.5 mm

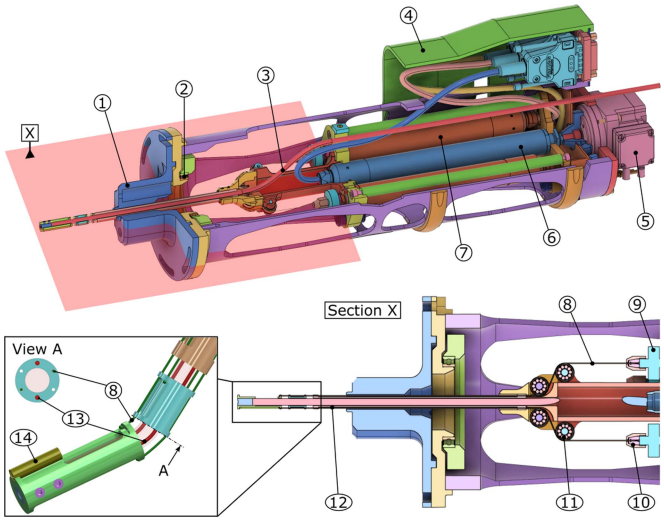

Fig. 3. Section view of the robot with detail of the compliant joint (1: Mount interface, 2: Bearing supporting the rotary frame, 3: Fibre optic, 4: Connection box, 5: Rotary actuator actuating the rotary frame (twist), 6: Linear actuator actuating the linear frame (feed), 7: Linear actuators actuating the tendons, 8: Tendons, 9: Load cells, 10: Collets, 11: Pulleys, 12: Articulated arm, 13: Nitinol rod, 14: CMOS camera).

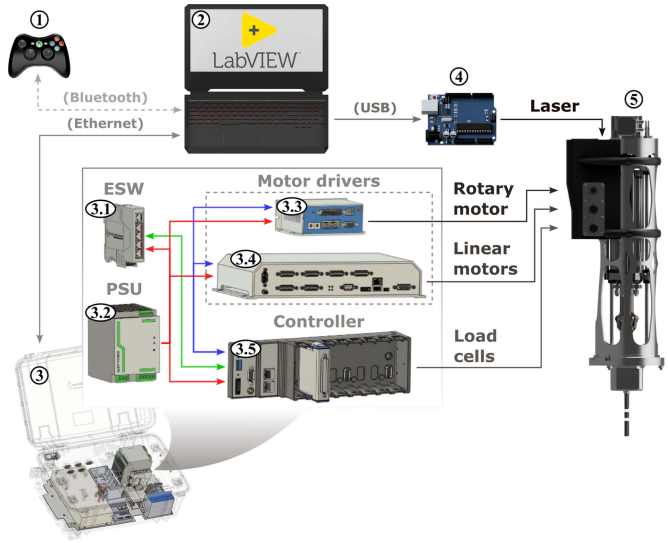

Fig. 4. Control hardware overview (1: Joystick, 2: Host PC, 3: Control unit, 3.1: Ethernet switch, 3.2: DC Power supply, 3.3: Rotary actuator drive, 3.4: Linear actuator drive, 3.5: Real-time controller, 4: Arduino, 5: Robot).

long and 120 mm in diameter. Including the articulated arm (fully retracted), the overall length of the robot is 507.5 mm for an overall weight of 4.4 kg. The Harmonic Drive FHA-8C-100-D200-EM1 actuator (4 in Fig. 3) drives the rotary unit and is installed on the outer chassis. This outer frame is equipped with a replaceable mounting interface (1) that permits the installation of the robot on different engines at various orientations. The inner rotary frame is connected on one hand to the rotary actuator and supported on the other by a deep groove ball bearing (2). The rotary frame has three linear guides over which the linear frame translates actuated by a PI L-220.50DG actuator (6). Within the linear frame, the four PI L-220.20DG linear actuators used to actuate the tendons are installed (7). The tendons (8), made of 0.44 mm stainless steel wire rope and connected to the actuators with stainless steel collets (10), are routed with a set of pulleys (11) through the articulated arm. The tension in the tendons is monitored with Omega LCM201-200 compression and tension load cells (9). Currently, the load cells are used to pretension the tendons, preventing slack during operation. In future, these will enable active tensioning during the operation, collision detection, and advanced control strategies such as haptic. Finally, a connection box (4) installed on the outer chassis contains the five D-sub connectors of the PI linear actuators and three industrial circular connectors for the Harmonic Drive rotary actuator and the sensors.

The details of the arm (12) are also shown in Fig. 3. Each compliant joints employs two Nitinol rods 0.69 mm in diameter installed 180° apart along the bending plane and is actuated by two tendons. The link design has been optimized for the specific application with an outer diameter of 8mm and an inner channel of 4.5mm, allowing the passage of the laser fiber optic and feed material. For this demonstration, the fibre-optic laser is replaced with a LC-LMD-650-01-01-A-C laser diode and a Misumi MD-V1001LH-120 miniature CMOS camera (14). When working with fiber optics, a key parameter to observe is the minimum bending radius to prevent damage and power losses. As shown in Fig. 3, the actuation unit and articulated arm were designed to provide an axial channel that minimizes the bending in the fiber. A minimum bending radius of approximately 50mm was achieved.

B. Control

1) Hardware: Fig. 4 provides a schematic overview of the control electronics. An Xbox controller (1) mapped to the key controls of the robot and the laser is used as the HMI. This communicates via Bluetooth to the host PC (2) on which the high-level non-real-time part of the control application runs. The host PC sends the operator's commands to the control unit (3), which takes care of the communication with actuators and sensors. An Arduino Uno (4) fitted with a custom circuit board receives serial commands from the host PC and powers the laser diode in sync with the robot's operations (5).

The NI cRio-9074 (3.5) acts as a master controller running the time-critical and deterministic part of the software. A NI-9237 strain/bridge input module is used to power the four load cells with an excitation voltage of 3.3 V, measure the output voltage of the Wheatstone bridge, and perform shunt calibration and offset null. The PI C-884.6DC (3.4) and the Copley Controls BEL-090-06 (3.3) drive respectively the five PI L-220 linear actuators and the Harmonic Drive rotary actuator. The safe torque off pin of the two controllers is wired to the emergency stop button, ensuring a means of disabling the actuators in case of critical failure of the control code. The Brainboxes SW-504 Ethernet switch (3.1) bridges together the various Ethernet devices, while the Phoenix Contact QUINT PS/1AC/24DC/20 (3.2) provides power to the whole unit.

2) Operation Workflow: As shown in Fig. 5, the system consists of a low-level (LLC) and high-level (HLC) control architecture. The LLC automatically starts when the control unit is powered up, with the cRio initiating communication with the motor drivers and sampling the sensors. When the operator starts the code on the host PC (HLC), the GUI is initialized and the connection with the LLC is established. (1)

IEEE Robotics and Automation Letters (RA-L) paper, presented at ICRA 2026, Vienna, Austria. Cite as RA-L paper.

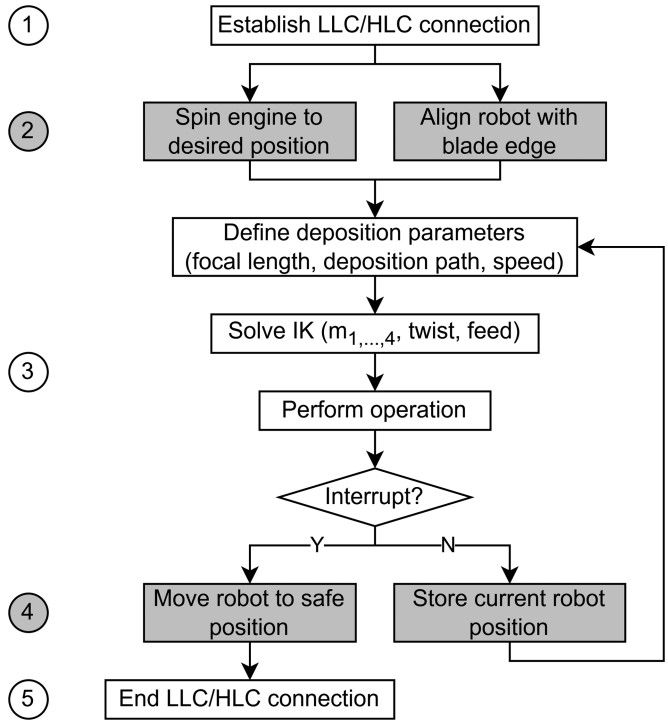

Fig. 5. Workflow of the operation (1: Connecting to the real-time controller, 2: Aligning the robot with the blade to repair, 3: Running the operation, 4: Retracting the robot, 5: Closing the connection with the real-time controller).

The GUI gives the user access to a variety of functionalities to control the system: jogging the robot, configuring and carrying out the automated AM operation, pretensioning the tendons, replacing the tendons, and calibrating the load cells via shunt calibration and null offset. During jogging, the DoFs of the robot can be controlled to move the end-effector to any point of the workspace, with the joint limits constantly monitored to prevent damage to the robot. The automated mode assists the user in achieving a high level of accuracy and repeatability during the AM operation. To achieve precise control of the tendon tension, a PID routine automatically pretensions the tendons by fine-adjusting the actuators' position until the desired tension is reached. This procedure, combined with the capability of actuating each linear actuator, also simplifies replacing a broken tendon, which represents the most common damage in tendon-driven systems.

Once the robot is installed on the engine and the rotor has been rotated such that the target blade is aligned with the borescope port, the repair operation can begin (2). First, the operator defines the process parameters such as laser focal length, deposition path in Cartesian space, and end-effector speed (Section II-D). Then, the inverse kinematics (IK) is solved to obtain the displacement of tendons ($m_{1,\dots,4}$), feed, and twist actuators (Section II-C); after this, the robot starts the automated routine. Throughout the entire operation, the visual feedback of an on-board camera (MISUMI MD-V1001LH-120 CMOS camera) can be used to ensure the process is proceeding correctly. If an anomaly is detected, the emergency stop can be actuated, interrupting the operation and activating the Safe Torque Off functionality of the motor drives. (3)

When the operation is completed, the robot retracts automatically to a safe position within the borescope port in which no collision with the blades can occur (4). The operator can then stop the HLC, closing the communication with the LLC and triggering closing routines such as storing the last state of the robot in non-volatile memory (5).

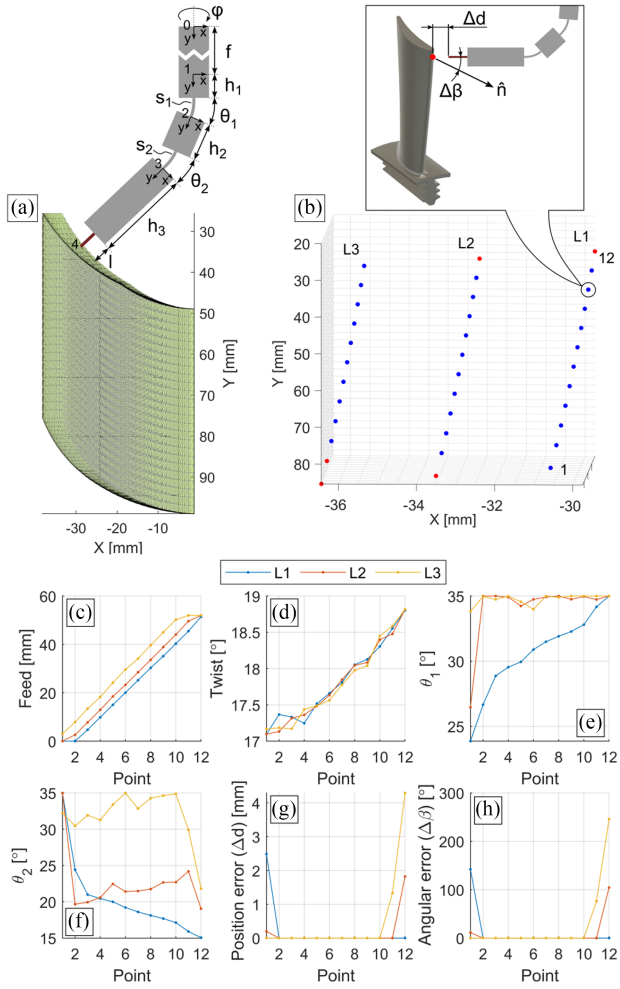

Fig. 6. Robot workspace and reachability analysis (A: Workspace shown as a 3D envelope, B: Points representative of a blade profile tested for reachability (blue reachable, red not reachable), C-F: Actuation variables (linear displacement and rotations) to reach the target points shown in B, G-H: Position and angular error with which the target points are reached).

C. Kinematics and Dimensional Synthesis

The kinematics description of the manipulator makes use of the piece-wise constant curvature (PCCK) formulation [19]. This approximates each compliant joint built with super-elastic rods with a continuous differential along the centerline of a theoretical backbone. Using the kinematic representation of the manipulator shown in Fig. 6(a), and temporarily disregarding the rotational (twist) and translational (feed) DoF along the articulated arm axis, which can be accounted for by an initial rotation and translation of the entire manipulator, a transformation matrix can describe each section:

$$ {}^{i}T_{i+1} = \begin{bmatrix} c_\theta & -s_\theta & 0 & \frac{s_i}{\theta_i}(c_\theta - 1) \\ s_\theta & c_\theta & 0 & h_i + \frac{s_i}{\theta_i} s_\theta \\ 0 & 0 & 1 & 0 \\ 0 & 0 & 0 & 1 \end{bmatrix} \tag{1} $$

IEEE Robotics and Automation Letters (RA-L) paper, presented at ICRA 2026, Vienna, Austria. Cite as RA-L paper.

where θ_i represents the rotation angle of each section, h_i the length of the rigid links, $c_\theta = \cos\theta_i$, $s_\theta = \sin\theta_i$, and s_i the arc length of the super-elastic element. The global transformation matrix used to calculate the FK from configuration to cartesian space can be written as:

$$ {}^0T_4 = {}^0T_1\,{}^1T_2\,{}^2T_3\,{}^3T_4 \tag{2}$$

in which ${}^0T_1$ accounts for the twist (angle of rotation: φ) and feed (displacement: f) at the base:

$$ {}^0T_1 = \begin{bmatrix} c_\varphi & 0 & s_\varphi & 0 \\ 0 & 1 & 0 & f \\ -s_\varphi & 0 & c_\varphi & 0 \\ 0 & 0 & 0 & 1 \end{bmatrix} \tag{3}$$

and ${}^3T_4$ for the focal length of the laser (l):

$$ {}^3T_4 = \begin{bmatrix} 1 & 0 & 0 & 0 \\ 0 & 1 & 0 & l \\ 0 & 0 & 1 & 0 \\ 0 & 0 & 0 & 1 \end{bmatrix} \tag{4}$$

While the full travel of the linear actuator (52 mm) was used for the feed (f), the twist angle (φ) was restricted to prevent damage to the tendon actuators' cables. Initial kinematic studies showed that given the linearity of a blade edge, the twist could be limited to 30° without affecting the reachability of the task space. Except for h_1 set equal to zero to have the first joint inside the engine when the robot is in the home configuration, the remaining kinematic variables were optimized using the task-oriented kinematic synthesis algorithm presented in [20], where it is also possible to find the mapping from configuration to actuation space. Having relaxed constraints in terms of minimum bending radius in the joints of the snake arm thanks to the use of a laser pointer instead of a fiber optic laser, the only technological constraint was on the length of the distal link that needed to accommodate the laser head and the camera. Values of 10mm for h_2, 25mm for h_3, and 4mm each for the two twin-pivot joints (s_1, s_2) were obtained. The suitability of these values was confirmed by investigating the capability of the robot to reach a set of representative points on the blade (Fig. 6(b)). In virtue of the linearity of the blade profile, a planar target workspace was built by translating the blade profile along the blade direction with an increment (Δ) equal to half of the notch depth.

Fig. 6 shows the robot workspace and summarizes the results of the reachability analysis. 36 points that represent the blade edge profile at different depths along the blade were considered. The robot is kinematically capable of reaching 31 (blue points in Fig. 6(b)) with a negligible error in position and orientation with respect to the blade normal (Fig. 6(g)–(h)). Having limited the bending angle of the twin-pivot joints to 35°, it is possible to observe from Fig. 6(c)–(f) that feed and joint angle should be increased if a larger workspace is desired. The 35° limit for the complaint joints was chosen to ensure that the nitinol element used in the joints didn't exceed the superelastic limit to prevent plastic deformation [21] and to guarantee a minimum short-term bend radius of the fibre optic of 6.55mm.

D. Path Planning for Blade Reconstruction

Fig. 7 provides a graphic representation of the path planning strategy to reconstruct the blade profile, in which the shape of the notch is simplified with a circular arc. The material is deposited layer-by-layer from the deepest point in the notch (B) to the edge profile (A-C).

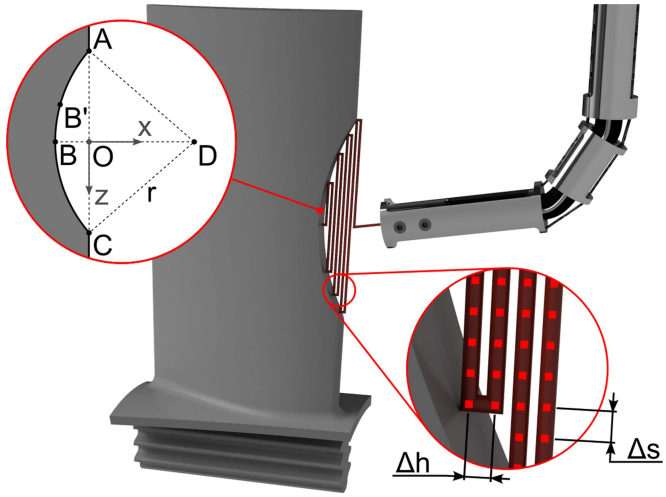

Fig. 7. Path planning strategy for blade reconstruction using parallel deposition lines within the notch profile.

The path generation algorithm begins with the operator jogging the robot to identify the notch's endpoints (A and C) and an intermediate point (B′). Their Cartesian coordinates are computed from actuator positions using the forward kinematics described in Section II-C, and can be expressed in either the robot base frame or a frame at the borescope port entrance.

From points A and C, it is possible to calculate a local frame centered at O:

$$ \vec{O} = \frac{1}{2}(\vec{A} + \vec{C}) \tag{5}$$

in which the z-axis is aligned with the blade edge, the y-axis is normal to the deposition direction, and the x-axis is defined using the right-hand rule based on the z and y axes:

$$ \hat{z} = \frac{\vec{AC}}{||\vec{AC}||} \tag{6}$$

$$ \hat{y} = \frac{\vec{OB'} \times \vec{OA}}{||\vec{OB'} \times \vec{OA}||} \tag{7}$$

$$ \hat{x} = \hat{z} \times \hat{y} \tag{8}$$

In this frame, the center of the notch D has y and z coordinates equal to zero ($y_D = z_D = 0$) so that the circumference can be fully defined by two of the three points:

$$ \begin{cases} (x_A - x_D)^2 + y_A^2 = r^2 \\ (x_{B'} - x_D)^2 + y_{B'}^2 = r^2 \end{cases} \tag{9}$$

and consequently:

$$ \begin{cases} x_D = \frac{x_A^2 - x_{B'}^2 + y_A^2 - y_{B'}^2}{2(x_A - x_{B'})} \\ r = \sqrt{x_D^2 + \vec{OA}^2} \end{cases} \tag{10}$$

Since $||\vec{OB}|| = r - x_D$, the position of $\vec{B}$ can be defined as $\vec{B} = (-||\vec{OB}||; 0; 0)$.

IEEE Robotics and Automation Letters (RA-L) paper, presented at ICRA 2026, Vienna, Austria. Cite as RA-L paper.

Algorithm 1: Path Planning.

Input: r, x_D, d, Δh, Δs
Output: p
$i \leftarrow 0$
for $d_i \leftarrow d - \Delta h$ **to** 0 **step** $-\Delta h$ **do**
  $z_{start} \leftarrow -\sqrt{r^2 - (d_i - x_D)^2}$
  $z_{end} \leftarrow -z_{start}$
  for $s_i \leftarrow z_{start}$ **to** z_{end} **step** Δs **do**
    $p(i) \leftarrow (d_i, 0, s_i)$
    $i \leftarrow i + 1$
  end for
end for

Defining the deposition depth, d, as the negative direction of the x-axis, i.e. the distance from point O in $\vec{OB}$ direction, a point on the notch profile has coordinate (0; 0; $\sqrt{r^2 - (d - x_D)^2}$). Therefore, if Δh is the layer height, i.e. the thickness of each deposited layer, and Δs is the distance between two points along the path, the path in cartesian space (p) can be obtained with a nested loop (Algorithm 1).

Finally, the inverse kinematics, solved using Sequential Quadratic Programming (SQP) [22], [23], can be used to derive the input for the actuators.

III. Experiments and Results

To validate the robot's performance and assess its suitability for high-repeatability tasks, three tests were conducted in controlled laboratory conditions: two using a VICON motion capture system with four Vantage 16 cameras (sampling rate: 30 Hz, calibration accuracy: 0.033 mm), and one inside a representative aeroengine.

While the position and angular accuracy requirements of the end-effector depend on the specific application, such as blade geometry and the AM setup, high repeatability remains highly desirable, as it enables consistent performance once the system is calibrated. To evaluate the intrinsic capabilities of the robot, an open-loop control strategy was employed. Nonetheless, further improvements in accuracy can be achieved through closed-loop control approaches, for example, by leveraging visual feedback from the onboard camera or incorporating shape sensors [10].

A. Motion Along the Linear Blade Edge

The profile of compressor blades, in particular for the early stages, is almost linear [20]. Accordingly, the reconstruction path is composed of multiple linear segments at varying depths within the notch profile. To evaluate the linearity and repeatability of the end-effector's motion, the robot was programmed to follow a linear trajectory along the edge of a blade in a 3D-printed section of a representative aeroengine. Fig. 8 shows the experimental setup. First, the robot was moved using the HMI to reach points P_1 and P_2, and their positions relative to the home position were stored in volatile memory. The trajectory of the end effector (l) was then programmed using a step of length $\Delta\lambda = 1\,mm$:

$$l(\lambda) = \vec{P_1} + \lambda(\vec{P_2} - \vec{P_1}) \tag{11}$$

As shown in Fig. 9(a), which compares the mean of 5 repetitions with the 3D best-fit line obtained using Principle Component Analysis [24] (VCN mean), the motion of the end

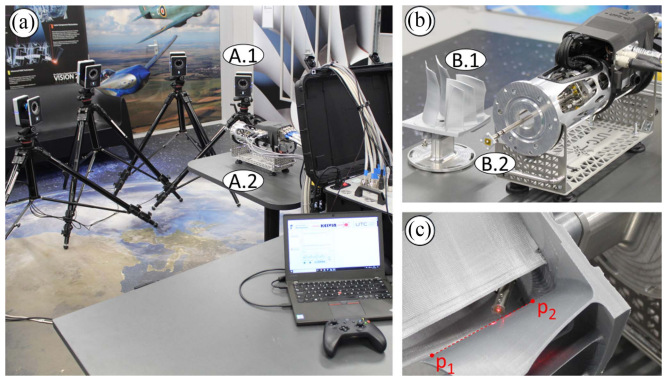

Fig. 8. Experimental setup to characterize the robot motion accuracy and repeatability (A: VICON motion capture setup, A.1: Cameras, A.2. Robot, B: Detail of the robot, B.1: Mockup of the blades in a representative stage of a aero engine, B.2: Motion capture markers installed on the tip of the robot arm, C: Motion along the blade edge).

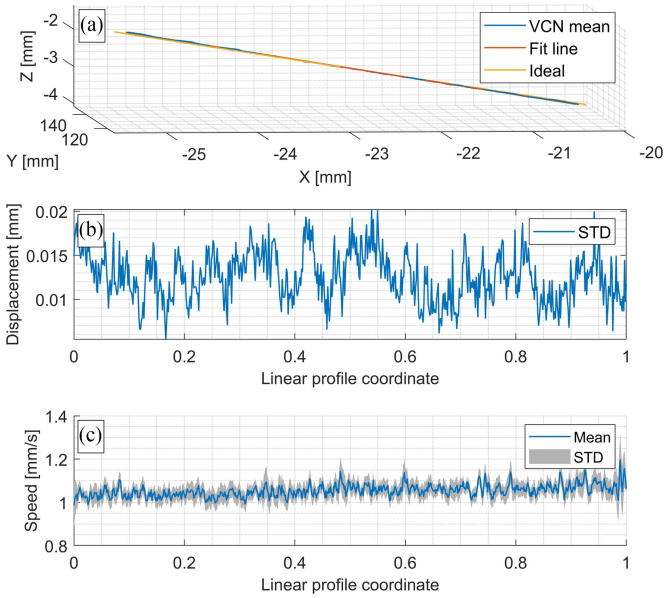

Fig. 9. Validation of the linear trajectory (A: Comparison between the experimental average position, best-fit line, and ideal trajectory; B: Standard deviation of the position over 5 repetitions; C: Mean and standard deviation of the end effector speed over 5 repetitions).

effector follows an almost perfectly linear path with a coefficient of determination (R^2) of the best-fit line of 0.999. In addition to the excellent linearity, the robot shows very good repeatability; Fig. 9(b) shows a value of the standard deviation of the Euclidean distance of the points recorded during the five repetitions from the centroids below 0.02mm. Finally, Fig. 9(c) shows the mean and standard deviation of the magnitude of the end effector's velocity, confirming the robot is capable of keeping a constant speed close to the commanded value of 1 mm/s.

B. Path for Simulated Blade Reconstruction

The performance of the robot on the path for reconstructing the blade was assessed using the same camera setup shown in

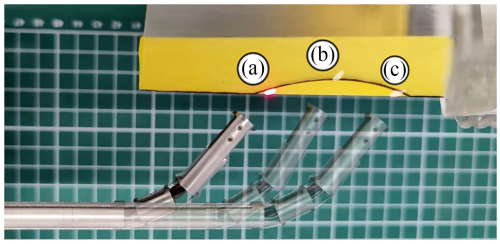

Fig. 10. Experimental setup used to record the three points (A, B, and C) for the path algorithm. The robot arm is shown moving along the notch profile.

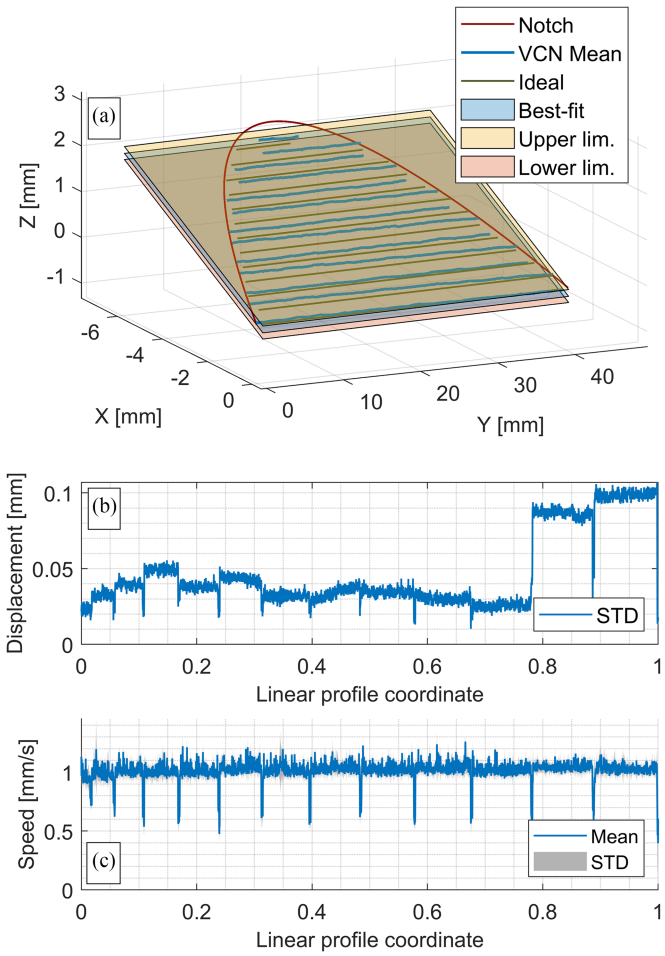

Fig. 11. Validation of the path for simulated blade reconstruction (A: 3D data (ideal and experimental) with best-fit planes to assess the planarity of the path; B: Standard deviation of the displacement over the 5 repetitions; C: Mean and standard deviation of the end effector speed over the 5 repetitions).

Fig. 8 and a 3D-printed blade to capture realistic values of the points A, B, and C along the notch profile (Fig. 10).

Selecting a path increment Δs equal to 1mm and a layer height Δh of 0.5mm, a path with 13 segments was generated. Once again, the linearity of the end effector motion along each segment was excellent, with an average R^2 value to the corresponding best-fit line of 0.999. The average distance between consecutive segments, measured as the distance between each segment's centroid, was 0.507 mm, a value close to the commanded Δh. Fig. 11(b) plots the standard deviation over 5 repetitions.

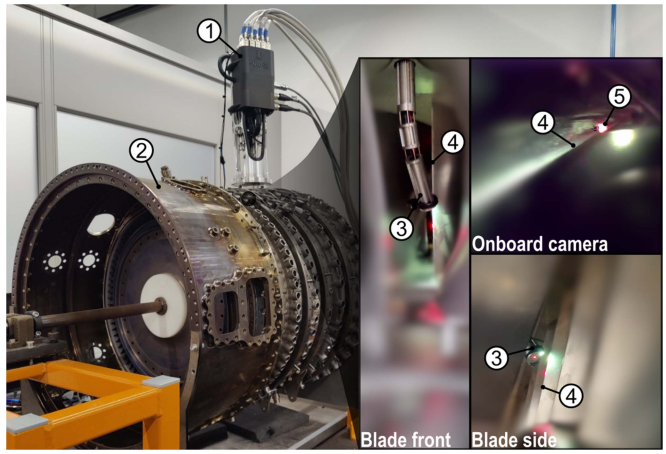

Fig. 12. Robot installed on an aeroengine with details of the laser pointer following the linear edge of a blade (1: Robot, 2: Aeroengine, 3: Articulated arm with laser diode and camera, 4: Blade edge, 5: Laser spot).

The robot showed very good repeatability (standard deviation below 0.055 mm) up to the last two segments, in which the standard deviation increases to 0.1 mm. These results can be explained kinematically, considering that the last segments reach the border of the robot's workspace, where the robot has lower manipulability. Another important metric for the reconstruction of the blade is the spread in the orthogonal direction to the best-fit plane. This aspect is important to ensure that, despite the limited width of the blade, the material is deposited on the thin blade edge. Fig. 11(a) gives a graphic representation of this, showing the planes parallel to the best-fit plane that contains all the points in the path. The average distance between the two limit planes was calculated to be 0.26 mm.

As shown in Fig. 11(c), the robot proved capable of maintaining the end effector stably close to the 1 mm/s programmed speed, with an average mean of 1.01 mm/s and a standard deviation of 0.05 mm/s. This result ensures the robot is capable of maintaining a constant flux of deposited material for a constant extrusion speed. It is worth observing that the troughs in the mean speed magnitude correspond to the passage from one segment to the next, consequently not representing a problem from a technological viewpoint.

C. *Visual Assessment Inside a Representative Aeroengine*

Having assessed the performance of the system for the AM process, a final test with a real aeroengine was carried out, performing all the steps the ground staff and operators would need to perform for a real repair.

Fig. 12 shows the robot installed on the engine case during operation. First, the borescope plug is removed and a mounting plate is connected to the borescope port. Then, the robot is bolted to the plate. The usage of an intermediate mounting plate makes the system universal, being able to operate on different engines. After having connected the robot to the control unit, the robot is ready to operate.

For this demo with the laser diode, the end-effector was programmed to follow the leading edge of one of the blades using the same algorithm described in Section III-A. Confirming the results obtained with the motion capture setup, the robot was

IEEE Robotics and Automation Letters (RA-L) paper, presented at ICRA 2026, Vienna, Austria. Cite as RA-L paper.

capable of guiding the laser successfully along the narrow blade edge (Fig. 12).

IV. Conclusion

This letter presents a new miniaturized tendon-driven manipulator for in-situ repair of aeroengine blades. The system represents a step forward toward the development of a portable system for in-situ additive manufacturing, combining the dexterity, multiple DoF, and miniaturized size that characterize a continuum robot with the requirements of high repeatability and technological needs, e.g. minimum bending radius of the fiber optics, required by direct laser deposition. The robot was developed with integrated actuation to make it fully portable and ready to be installed on a variety of aeroengines just by selecting the appropriate interface. The electronics, ruggedized and housed in a portable case, can be connected to any laptop running the lightweight GUI, making it ideal for operating in actual industrial environments.

Extensive experimental characterization confirmed excellent linearity and repeatability of the end-effector on a linear path. The robot performed well also on a path simulating the reconstruction of a blade, both in terms of repeatability and path shape. While the required end-effector accuracy depends on the specific use case (blade geometry and AM setup), the repeatability below 0.2 mm achieved with open-loop control is promising and suggests that high accuracy can be reached through suitable calibration procedures. In addition, the end effector maintained a sufficiently constant velocity, a parameter important to ensure a homogeneous amount of material deposited. It is worth noting that the tests were conducted in controlled laboratory conditions; additional work will be required to ensure applicability to real-world scenarios where disturbances may affect the robot's performance.

Other than the specific system presented, this letter provides insight into the key aspects to consider when developing a system for in-situ AM operations, such as mechanical and electronics considerations to make the system portable, kinematic optimization for the specific task, and extensive testing in realistic scenarios. These aspects, if carefully implemented, could help in further fostering the use of robotics in 3D printing and developing new, more portable systems.

Future research will focus on improving the kinematic modeling of the articulated arm, departing from the constant curvature assumption to reduce the position error compared to the theoretical path. Furthermore, closed-loop control using, for example, the visual feedback from the camera and the feedback from the load cells will be explored to improve the robot's accuracy. Finally, tests with the actual laser head will be carried out to optimize process-specific parameters.

References

[1] D. Alatorre et al., "Robotic Boreblending: The future of in-situ gas turbine repair," in *Proc. 2018 IEEE/RSJ Int. Conf. Intell. Robots Syst.*, 2018, pp. 1401–1406.

[2] I. Gibson, D. Rosen, B. Stucker, and M. Khorasani, *Directed Energy Deposition*. Cham, Switzerland: Springer, 2021, pp. 285–318.

[3] J. M. Wilson, C. Piya, Y. C. Shin, F. Zhao, and K. Ramani, "Remanufacturing of turbine blades by laser direct metal deposition with powder," *J. Cleaner Prod.*, vol. 80, pp. 170–178, 2014.

[4] D. Wu, J. Liang, H. Wang, and J. Yu, "Investigative on the remanufacturing process of TC4 blade based on selective laser melting and CNC machining," *J. Mater. Res. Technol.*, vol. 21, pp. 450–464, Nov. 2022.

[5] B. Blakey-Milner et al., "Metal additive manufacturing in aerospace: A review," *Mater. Des.*, vol. 209, Nov. 2021, Art. no. 110008.

[6] A. Saboori, A. Aversa, G. Marchese, S. Biamino, M. Lombardi, and P. Fino, "Application of directed energy deposition-based additive manufacturing in repair," *Appl. Sci.*, vol. 9, no. 16, Aug. 2019, Art. no. 3316.

[7] M. K. Keshavarz, A. Gontcharov, P. Lowden, A. Chan, D. Kulkarni, and M. Brochu, "Turbine blade tip repair by laser directed energy deposition additive manufacturing using a rene 142–MERL 72 powder blend," *J. Manuf. Mater. Process.*, vol. 5, no. 1, Mar. 2021, Art. no. 21.

[8] B. Rottwinkel, C. Nölke, S. Kaierle, and V. Wesling, "Crack repair of single crystal turbine blades using laser cladding technology," *Procedia CIRP*, vol. 22, pp. 263–267, 2014.

[9] D. Alatorre et al., "Teleoperated, in situ repair of an aeroengine: Overcoming the internet latency hurdle," *IEEE Robot. Autom. Mag.*, vol. 26, no. 1, pp. 10–20, Mar. 2019.

[10] M. Russo et al., "Continuum robots: An overview," *Adv. Intell. Syst.*, vol. 5, 2023, Art. no. 2200367.

[11] X. Dong et al., "Continuum robots collaborate for safe manipulation of high-temperature flame to enable repairs in challenging environments," *IEEE/ASME Trans. Mechatron.*, vol. 27, no. 5, pp. 4217–4220, Oct. 2022.

[12] Z. Yang, L. Yang, Y. Sun, and X. Chen, "A novel contact-aided continuum robotic system: Design, modeling, and validation," *IEEE Trans. Robot.*, vol. 40, pp. 3024–3043, 2024.

[13] Q. Qi et al., "Design and motion control of a tendon-driven continuum robot for aerospace applications," in *Proc. Inst. Mech. Engineers, Part G: J. Aerosp. Eng.*, vol. 238, no. 13, pp. 1296–1310, 2024.

[14] J. Burgner-Kahrs, D. C. Rucker, and H. Choset, "Continuum robots for medical applications: A survey," *IEEE Trans. Robot.*, vol. 31, no. 6, pp. 1261–1280, Dec. 2015.

[15] P. E. Dupont, N. Simaan, H. Choset, and C. Rucker, "Continuum robots for medical interventions," in *Proc. IEEE*, vol. 110, no. 7, pp. 847–870, Jul. 2022.

[16] I. Surgical, "Intuitive da vinci," 2024. [Online]. Available: https://www.intuitive.com/en-us/products-and-services/da-vinci

[17] F. Wang et al., "FIORA: A flexible tendon-driven continuum manipulator for laparoscopic surgery," *IEEE Robot. Automat. Lett.*, vol. 7, no. 2, pp. 1166–1173, Apr. 2022.

[18] D. A. Troncoso et al., "A continuum robot for remote applications: From industrial to medical surgery with slender continuum robots," *IEEE Robot. Automat. Mag.*, vol. 30, no. 3, pp. 94–105, Sep. 2023.

[19] I. Robert, J. Webster, and B. A. Jones, "Design and kinematic modeling of constant curvature continuum robots: A review," *Int. J. Robot. Res.*, vol. 29, no. 13, pp. 1661–1683, 2010.

[20] M. Russo, L. Raimondi, X. Dong, D. Axinte, and J. Kell, "Task-oriented optimal dimensional synthesis of robotic manipulators with limited mobility," *Robot. Comput.- Integr. Manuf.*, vol. 69, 2021, Art. no. 102096.

[21] L. Raimondi, M. Russo, X. Dong, and D. Axinte, "Understanding friction and superelasticity in tendon-driven continuum robots," *Mechatronics*, vol. 104, 2024, Art. no. 103241.

[22] Y. Huang et al., "An efficient computational approach for inverse kinematics analysis of the UR10 robot with SQP and BP-SQP algorithms," *Appl. Sci.*, vol. 13, no. 5, 2023, Art. no. 3009.

[23] S. Xie, L. Sun, Z. Wang, and G. Chen, "A speedup method for solving the inverse kinematics problem of robotic manipulators," *Int. J. Adv. Robot. Syst.*, vol. 19, no. 3, 2022, Art. no. 17298806221104602.

[24] I. T. Jolliffe and J. Cadima, "Principal component analysis: A review and recent developments," *Philos. Trans. Roy. Soc. A: Math. Phys. Eng. Sci.*, vol. 374, no. 2065, 2016, Art. no. 20150202.